Open Access Library Journal
2026, Volume 13, e15274
ISSN Online: 2333-9721
ISSN Print: 2333-9705

Global Zones of Particle Precipitation: EXOS-C's Observation

Miah Muhammad Adel

Department of Chemistry & Physics, University of Arkansas at Pine Bluff, Pine Bluff, AR, USA
Email: adelm@uapb.edu

How to cite this paper: Adel, M.M. (2026) Global Zones of Particle Precipitation: EXOS-C's Observation. *Open Access Library Journal*, **13**: e15274.
https://doi.org/10.4236/oalib.1115274

Received: March 30, 2026
Accepted: May 25, 2026
Published: May 28, 2026

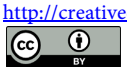

Abstract

This article pertains to EXOS-C's LEO observations during 1984-1986 of quasi-trapped protons (0.64 - 35 MeV) and electrons (0.19 - 3.2 MeV) with the main focus on the former. The temporal variation of proton population near the geomagnetic equator reveals that the peak value of the equatorially mirroring component may increase by a factor of 50 or more between a solar maximum and a minimum condition, and that the peak flux profile of protons in the equatorial, low latitude, midlatitude, and auroral zones lying to the north and south of the equator, exist in parallel with the minimum magnetic field equator. Further, the proton and the electron populations in the said midlatitude zone show longitude and altitude dependencies. The locations of the peak profiles in all three zones in L-space depend upon the pitch angles of particles the distribution of which shows a second peak in addition to the one at 90˚ pitch angle. Particle flux does not depend on the local time. However, there is a great seasonal variation in e and p fluxes, possibly due to the solar condition. Particle flux variations are indicative of the presence of scattering by electromagnetic waves generated by both solar wind disturbances and magnetospheric instabilities. These waves and the ring current particles interact to redistribution of particles spatially and energy-wise. The energy spectra of both p and e fluxes run almost parallel. Theoretical understanding of these observations is in progress with the work of data analysis of other parts of the global zones.

Subject Areas

Astrophysics

Keywords

EXOS-C, LEO, SEPs, Magnetosphere, Response Function, Absolute Flux, L-Parameter

1. Introduction

NASA focuses on multiple observations-pertaining data analysis, data-model comparison, and theory among others pertaining to the description of magnetospheric structure and evolution. The agency targets current and historical data bases from *in situ* spacecraft observations and/or extended.

LEO observations to build innovative data-based specification and prediction capabilities for the global magnetosphere. It will apply data assimilation tools and methods. The study will link solar wind perturbations to global changes in the magnetospheric structure and solar energetic particle fluxes, perturbations of the ionosphere and thermosphere, radiation belts, and geomagnetically induced currents. This article pertains to EXOS-C's LEO observations that use historical databases (https://nspires.nasaprs.com/external/solicitations/summary!init.do?solId=%7B274C8365-A038-339F-A3AE-8F5BFE178312%7D&path=&redirectURL=). While the NASA's satellites report recent observations, this article reports synergistically some unreported observations made by the Japanese EXOS-C satellite in the 1980s covering some of NASA's stipulations.

The Sun couples with the Earth through the interactions of solar energetic particles (SEP) released in solar flares (SFs) and coronal mass ejections (CMEs) [1]-[10]. The strongest geomagnetic storms (GSs) are usually generated by the interaction of the magnetosphere with an incoming ICMEs ejection plasma and the associated magnetic field [11]-[13] characterized by entrance of energetic electrons and ions into the inner magnetosphere [14]-[29]. Papaioannou [30] prepared a catalog of 314 SEP-events spanning 1984-2013 based on Geostationary Operational Environmental Satellite (GOES)/Energetic Particle Sensor (EPS) data [31]. SEPs propagate in the interplanetary space along the lines of force of the interplanetary magnetic field. Solar transient events can be cross-platform analyzed using data from solar, heliospheric, and magnetospheric missions along with ground-based instruments from different sources for SEP prediction, geomagnetic storm influence on the ionosphere, the response of the different magnetospheric current systems to the ICME arrival, the dynamics of the plasmasphere during the different phases of the geomagnetic storm [31]-[35]. The reported investigation is an unpublished work on the global zones of particle precipitation that was under the SEPs from SFs and CMEs as studied by the Japanese OHOZORA satellite during 1984-1986.

Charged particle detectors whether the solar energetic/magnetospheric particles detectors or space weather observing onboard have conical telescopes with some opening angles like the particle detection instruments on EXOS'C. Incident particles—electrons and ions—interact with the surface. The analysis of the mass, energy and/or trajectory of the emitted particles is used to identify the incident particles indirectly.

Parker Solar Probe was launched on 12 August 2018 for a mission duration of 7 years. SWEAP (Solar Wind Electrons Alphas and Protons) on board the space craft counts the electrons, protons and helium ions, and measure their properties

such as velocity, density, and temperature.

Advanced Composition Explorer (ACE) [36] was launched in August 1997. The Electron, Proton, and Alpha Monitor (EPAM) on board made measurements of 40 - 350 keV electrons and 46 - 4800 keV energetic particles in specie groups of H, He, CNO, and Fe. It was still operating as of 2023.

Voyager 1 was launched on 5 September 1977. It is the most distant human-made instrument in deep space [37]. It has low energy charged particle instruments (LECP) to measure the differential in energy fluxes and angular distributions of ions, electrons and the differential in energy ion composition.

GOES 16 was launched on November 19, 2016, for planned 15 years duration to detect energetic heavy ions, low, medium, and high energy magnetospheric electrons and protons, and solar and galactic protons.

Van Allan Probe A and Van Allen Probe B were launched on August 30, 2012 to detect energetic particle composition and thermal plasma, radiation belt storm probes ion composition, relativistic protons, and electric field and waves. The space crafts were deactivated before the end of 2019.

The Energetic Particle Telescope (EPT) was accommodated on board the PROBA-V satellite launched on May 7th, 2013 to detect electrons (0.2 - 10 MeV), protons (4 - 300 MeV), alpha particles (16 - 1000 MeV), and heavier ions (up to 300 eV/nucleon). The mission's planned maximum lifetime was 5 years.

2. Methodology

Electron and proton count rates were overviewed for quality data, and pole-to-pole satellite passes falling within ±80˚ geomagnetic latitudes were separated. Previously developed software was revised, and some new software was developed, tested, and applied to decode data of both the differential and integral proton and electron channels, pertaining to the low-latitude, mid-latitude, and auroral zones lying on the northern part of the equator. The data were then cleaned of contaminations, especially for rate spikes. Most of the time was devoted to the mid-latitude zone e and p data. Some features of the low-latitude zone, too, were studied.

Average values of particle count rates R, geomagnetic latitude λ, geomagnetic longitudes φ, pitch angles α, altitude h, magnetic field B, McIlwain's parameter L, local time t_{lcl}, and magnetic local time t_{mgblcl} spanned in 1˚-latitude latitude bin were calculated. Combined plots were made of average particle count rates R_{avrg} vs the average values of λ, φ, α, h, B, L, t_{lcl}, and t_{mglcl}. Then separate plots were made of $R_{peak\ avrg}$ vs other variables.

3. Spatial Features

3.1. Survey Plots

The rate spikes were detected by making plots for individual satellite passes of the average counting rates per 1˚ latitude bins vs latitude, longitude, altitude, L, B, local time, and the angle between the telescope axis and the magnetic field

direction (χ). Figure 1(a) and Figure 1(b) show such plots. In these figures, the quantities along the horizontal axis are also the average values over 1˚ latitude bin. The zero values along this axis are to be ignored. They simply indicate the terminating position for the given pass number. The broken lines indicate protons and the solid lines electrons. Counted from the left-hand side the first peak is for the low-latitude region, the second peak for the mid-latitude region, and the third for the auroral region. These plots have helped (i) to identify the magnitudes and locations (in all the parameters along the horizontal maxis) of the peak counting rates, (ii) to identify the peaks and extent of the respective region, and (iii) to discard the data for a particular region for a given pass if contaminated by rate spikes.

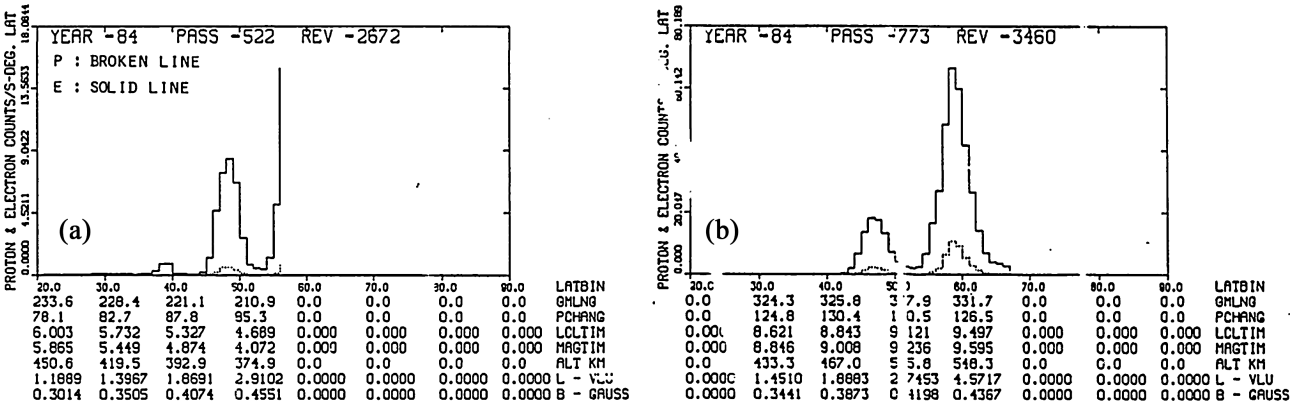

Figure 1. (a) Survey plot of electrons (solid line) and protons (broken line); (b) Survey plot of electrons and protons.

3.2. Global Profile

The global peak flux profile of protons in the three zones is shown in Figure 2(a) (leftmost). This figure shows distinctly the plots of latitude vs longitude of the locations of the peak counting rates. Figure 2(b) (middle) shows the global peak flux profile of all the six zones. Figure 2(c) (rightmost) shows the global profile of the minimum magnetic field equator. It is evident that the proton peak flux profiles in the three zones in the northern hemisphere and the two zones in the southern the run parallel to the minimum magnetic field profile.

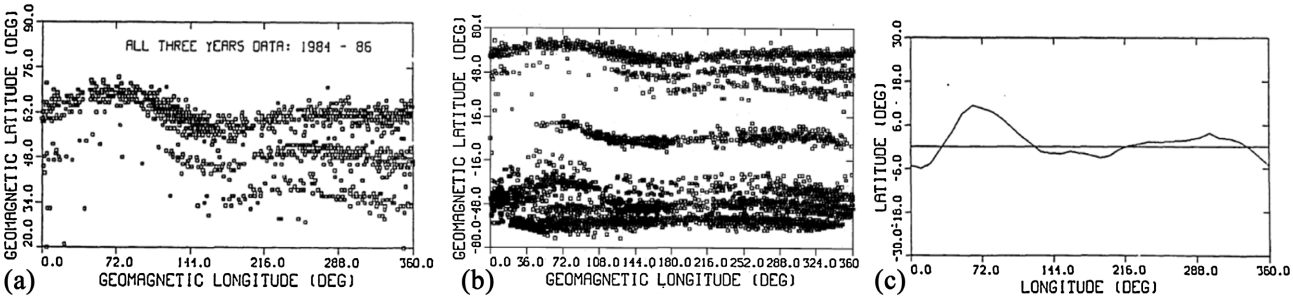

Figure 2. (a) Global peak flux profiles of protons in the northern hemisphere; (b) Global peak flux profiles of protons in the northern and southern hemispheres; (c) Minimum geomagnetic equator.

The particle clustering can happen in their latitudes λ_M which is related to their equatorial pitch angles α_e via

$$\sin^2 \alpha_e = \cos^6 \lambda_M \Big/ \left(1+3\sin^2 \lambda_M\right)^{0.5} \tag{1}$$

which can be approximate to

$$\sin \alpha_e \approx \cos^4 \lambda_M \tag{2}$$

The angles of the low-latitude around 28˚, midlatitude 12˚, and auroral zone 3˚. And the mirror point field values as obtained from

$$B_M = B_e \big/ \sin^2 \alpha_e \tag{3}$$

are 1.4 μT, 7.2 μT, and 113 μT, respectively.

Exospheric thermal neutral hydrogen causes charge exchange interactions with the ring current particles making this their primary loss mechanism. For particles mirroring at a latitude λ_M the charge exchange lifetime is given by

$$\tau_M = \left(\cos\left(\lambda_M\right)^i\right) \Big/ \left(n\left(r_o\right)\sigma_{10}\left(E\right)v\right) \tag{4}$$

where τ = mean lifetime of protons or other ring current species confined in the equatorial plane,

$n(r_o)$ = exospheric hydrogen in the equatorial plane,

v = velocity of the ion

$\sigma_{10}(E)$ = hydrogen atom charge exchange cross section of the ion with the neutral [38]

$$i = 3.5 \pm 0.2 \tag{5}$$

indicating that off-equatorially mirroring particles do not charge exchange rapidly.

Ring current particles interact with cold plasma of the plasma sphere creating intense ion cyclotron turbulence [39]. This wave causes pitch angle scattering. Williams *et al.* [40] showed that the pitch angle scattering is an efficient way of ring current energy deposition in the atmosphere. The second peak in the survey plots may be attributed to this cause.

4. Temporal Variation of Protons in the Equatorial Zone

Proton flux varied enormously with the solar maximum and minimum conditions. The energy range of protons extends from the energy of quasitrapped to stably trapped protons. Some reasoning has been used to estimate the fraction of quasitrapped protons in that energy range. Further, in order to show the energy spectra and the mean energy, comparison has been made of the EXOS-C observations with the observations made at both the low and high energy ends of the energy range in the comparable altitude and *L*-range near the equator. We take help of the observations at the low energy end [41]-[47] and at the high energy end [37]-[45].

4.1. Quasi-Trapped Component

In Figure 3, we have compiled data of both low and high energy protons from the previous observations. We have covered the energy range of less than 10 keV to 35 MeV comprising post-storm, pre-storm, and average geomagnetic conditions. Dial data. [45] are represented by the three curves to the right side beyond 5 MeV corresponding to, from the bottom, L = 0.98, 1.02, 1.08, 1.14, and 1.18. The other two horizontal lines at 1.3 MeV are from Phoenix-1 observation [48]-[51] the bottom line is the observed flux at 277 km and the top line for the extrapolated flux at 450 km based on altitude dependence. The equatorial perpendicular peak flux of protons shows an L dependence of ~ L^{81} [45] [46] in the energy range of ~5 MeV to beyond the higher energy end of the S-1 integral energy channel. The L-dependence of S-1 measured perpendicular peak flux of protons is only $L^{4.25}$ as has been reported above. The very low power law index of 4.25 compared to the large index of 81 indicates that the portion of higher energy component of protons in flux is negligible compared to the lower energy quasi-trapped component. The next subsection estimates it to be nearly one-quarter of the low energy population if 5 MeV (based on available measurements) is taken as the upper limit of the low energy component.

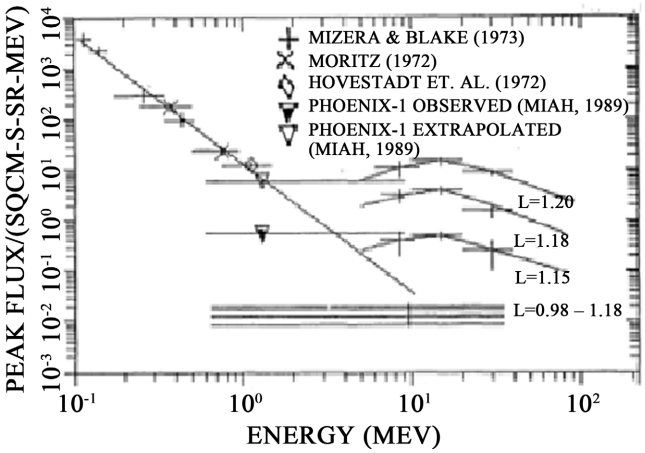

Figure 3. Energy spectra of protons.

4.2. Mean Energy of the Protons

Following the observations of L-independence of low energy particles [43]-[51], we have plotted the low energy (10 keV < E < 2 MeV) equatorial flux in the L range of 0.98 to 1.14. A least square fit to the data describes the flux by the power-law exponent ~2.55 [48]-[51]. Without any anticipation of abrupt changes, we assume the power-law $E^{-2.55}$ to be valid at 1 to 1.15 for low energy protons up to 5 MeV. This inclusion does not affect the integral energy flux significantly because of the steep nature of curve. In the wide range of observation, Dial [45] data at L = 1.15 fits $E^{0.4}$ for 5 ≤ E ≤ 15 MeV and $E^{-1.0}$ for 15 ≤ E ≤35 MeV. At this L-shell, the proportion of the integral energy fluxes in the three intervals are shown in Table 1 below.

Table 1. Energy range wise integral energy flux.

Energy interval (MeV)	Power law	Flux ($cm^{-2}\cdot sr^{-1}\cdot s^{-1}$)
0.64 - 5.0	$E^{-2.55}$	16.00
5.0 - 15.0	$E^{0.4}$	4.22
15.0- 35.0	$E^{-1.0}$	2.70

The integral energy flux observed by EXOS-C at L = 1.15 is 0.62 $cm^{-2}\cdot s^{-1}\cdot sr^{-1}$. The proportions shown in Table 1 yield 0.433 $cm^{-2}\cdot s^{-1}\cdot sr^{-1}$ in the range 0.64 to 5 MeV, 0.114 $cm^{-2}\cdot s^{-1}\cdot sr^{-1}$ in 5 to 15 MeV, and 0.073 $cm^{-2}\cdot s^{-1}\cdot sr^{-1}$ in 15 to 35 MeV. The mean energy of the protons from the integration of the weighted normalized power laws in three different regions was found to be 9.53 MeV. The bottom four horizontal lines are drawn with the full energy range of the EXOS-C energy channel. For comparison, normalized law $E^{-2.55}$ law alone leads the mean energy to be 5.69 MeV.

4.3. Flux Discrepancy

A striking point in the plot is the low value of the flux observed in the S-1 telescope. This flux is 27.8 times lower than the power law predicted value ($0.64 \le E \le 35$ MeV), 7.7 times lower than the Phoenix-1 [48]-[51] observed flux ($0.6 \le E \le 9.1$ MeV) at 277 km, and 87.7 times lower than the Phoenix-1 extrapolated flux at 450 km. The flux ($cm^{-2}\cdot s^{-1}\cdot sr^{-1}$.) comparison is shown in Table 2.

Table 2. Comparison of flux.

Power law predicted	Phoenix-1 observed at 277 km	Phoenix-1 extrapolated to 45 km	EXOS-C observed
16.7	4.64	52.7	0.60

The actual flux comparison needs involvement of the instrument response function which is not the same for all the telescopes at the geomagnetic equator. We postpone the explanation of this flux decrease in 1984-1986 until we have compared absolute fluxes during the epochs of observations in 1982 and 1984-1986.

4.4. Instrument Response Function

The study of the temporal variation of flux for the same instrument at different times is much easier than when the comparison involves among measurements made by different instruments because of the calculation of the response function of the instrument to particles of different pitch angles. We calculate the changes of absolute flux between the epochs of 1982 when the Sun was very violent and 1984-1986 when the Sun was passing through a solar minimum. The particle counting rate R of a detector of area A having the efficiency function $f(\alpha)$ between the energy ranges E_1 and E_2 for the spectrum $E^{-\delta}$, and the pitch angle range α_1

and α_2 for the pitch angle distribution characterized by $\sin^q\alpha$ at the magnetic field B, the magnetic shell L, latitude λ, longitude φ, and time t is given by [49]-[52].

$$R = (1/T)\int \mathrm{d}t \int \mathrm{d}E\, E^{-\delta} \int \mathrm{d}\omega \int \mathrm{d}\boldsymbol{A}\cdot\boldsymbol{r}(\omega)\cdot J_n(B,L,\lambda,\phi,q,t) \tag{6}$$

To evaluate the integral numerically, we split into parts which yield

$$R = AFJ_nQ \tag{7}$$

$$\text{where} \quad F = \int \sin^q \alpha f(\alpha)\mathrm{d}\alpha \tag{8}$$

with limits α_1 and α_2,

$$\text{and} \quad Q = \int E^{-\delta}\mathrm{d}E \tag{9}$$

with limits E_1 and E_2. The efficiency function $f(\alpha)$ can be evaluated for the telescopes (49). For illustration, the efficiency functions of all three telescopes in AZUR, S81-1, and EXOS-C have been plotted in **Figure 4**. AZUR telescope has the smallest efficiency function in the smallest equatorial pitch angle range. The next one is S81-1 telescope on board the S81-1 mission has the largest efficiency, and is the largest relative to 2π, the efficiency function of a plane detector. Sine function raised to some exponents can be used to fit the efficiency function. Equation (8) can be evaluated numerically. Equation (7) lets us calculate J_n from the counting rates, detector area, integral of the product functions of pitch angle distribution, the response function, and the integral spectrum. From Equation (7), the normalization constant J_n which is representative of the actual flux can be calculated.

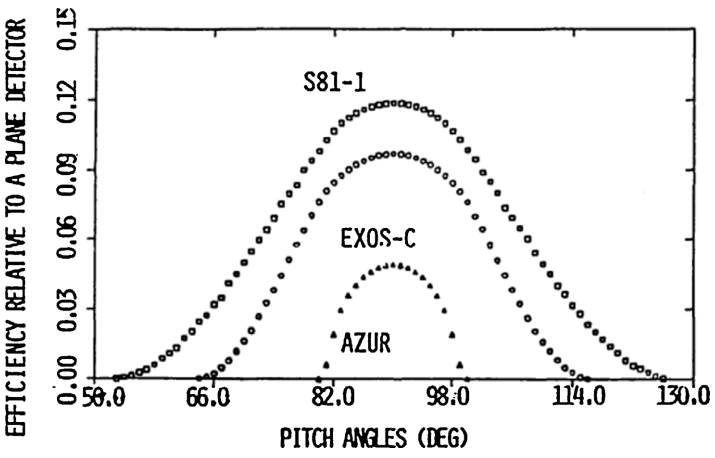

Figure 4. Instrument response function to particles of different pitch angles.

We have plotted the instrument response functions of the S-1 telescope on board EXOS-C for several orientations of the telescope axis with respect to the magnetic field direction, *i.e.* for different values of the angle χ. Later part of the report will refer to these plots. **Figures 5(a)-(f)** illustrate the instrument efficiency functions. While no direct relation between the counting rates and the efficiency function is illustrated here, the figs. distinctly show that between the efficiency function and the angle χ.

Figures 5(a)-(f) Plots of response functions vs pitch angle for different orientations of the telescope axis with respect to the magnetic field direction. This angle has been designated by χ_i. χ_i values are gradually decreasing for the solid curves from 90˚ to 40˚ degrees and increasing for the dotted curves 90˚ - 140˚.

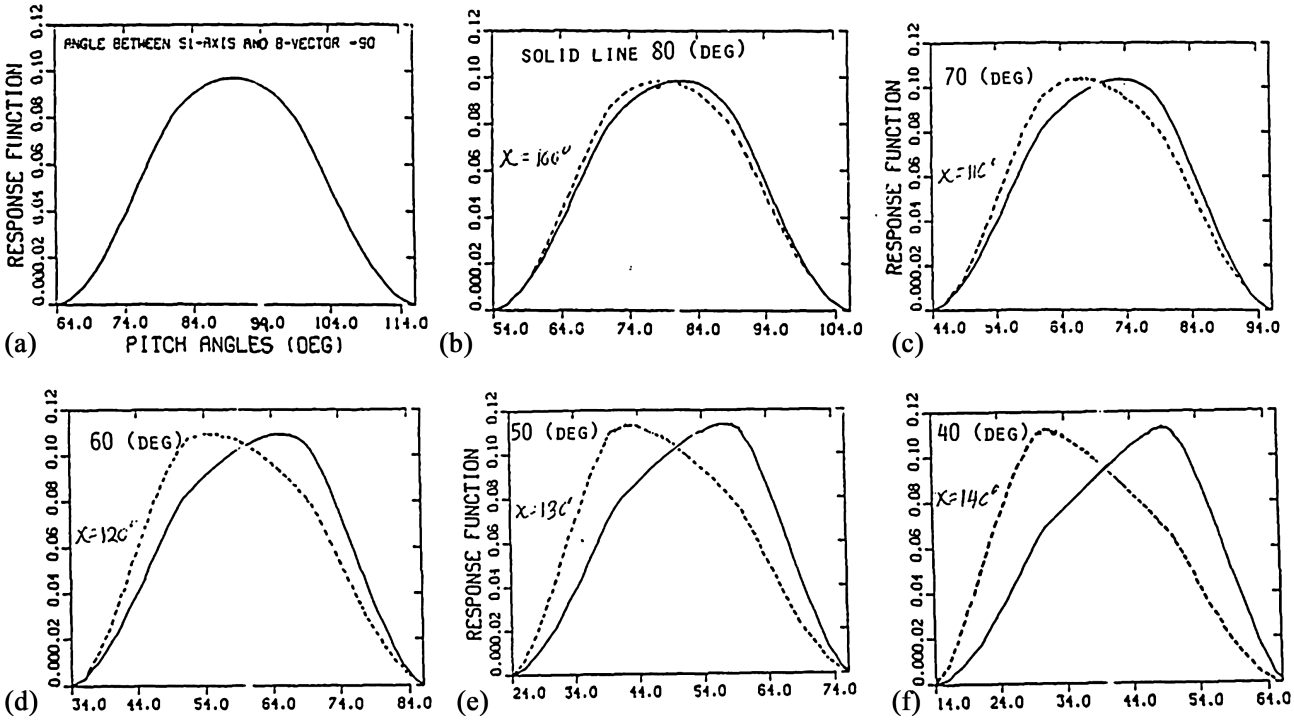

Figure 5. (a) Pitch angle response function of S-1 telescope for $\chi = 90^\circ$ angle between the telescope axis and the magnetic B vector; (b) Pitch angle response function of S-1 telescope for $\chi = 80^\circ$ angle between the telescope axis and the magnetic B vector; (c) Pitch angle response function of S-1 telescope for $\chi = 70^\circ$ angle between the telescope axis and the magnetic B vector; (d) Pitch angle response function of S-1 telescope for $\chi = 60^\circ$ angle between the telescope axis and the magnetic B vector; (e) Pitch angle response function of S-1 telescope for $\chi = 50^\circ$ angle between the telescope axis and the magnetic B vector; (f) Pitch angle response function of S-1 telescope for $\chi = 40^\circ$ angle between the telescope axis and the magnetic B vector

4.5. Comparison of Absolute Flux

For comparison of absolute fluxes, we have plotted J_n in **Figure 6** for the known values of q. The dependence of J_n upon other variables is not significant [48] [49]. The bottom curve marked with circles is for EXOS-C observation. The second curve from the bottom marked with triangles is AZUR's observation. The third curve marked with triangles is Phoenix-1 data. The fourth curve marked with crosses is the Phoenix-1 data predicted by the source depletion model [48]-[51]. The top curve marked with squares is 19.5, 39.6, 59.4, 420.5 times less than AZUR, Phoenix-1, Phoenix-1 extrapolated flux, respectively. **Figure 6**, in essence, compares the absolute population of quasi-trapped particles in the equatorial thermosphere.

4.6. Impact of Solar Condition

The fact that the absolute flux in 1984-1986 is 40 times less than that in 1982 [49] or that in 1969-1970 [43] warrants our special attention. We have seen in Equation. (7)

that J_n remains to be a function of t, i. e. epoch. The large variation is probably because of the solar condition. The Sun was passing through a maximum condition in 1982 and a minimum in 1984-1986 as shown in Figure 7 [53]. During the solar maximum conditions, the radiation particle intensity increases. Further, light gases escape to exosphere more during the maximum conditions as shown in Figure 8

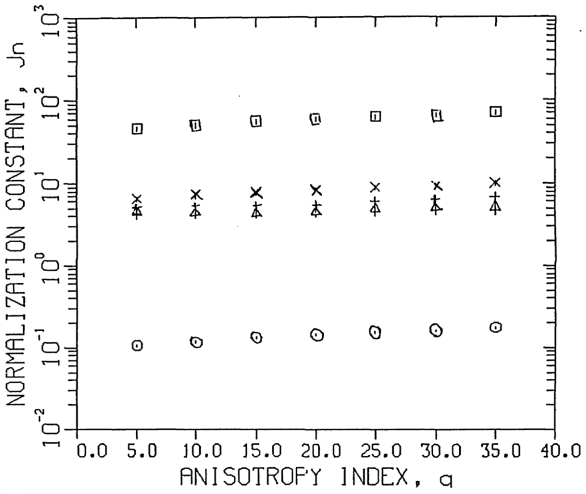

Figure 6. Normalization constant variation with the anisotropic index.

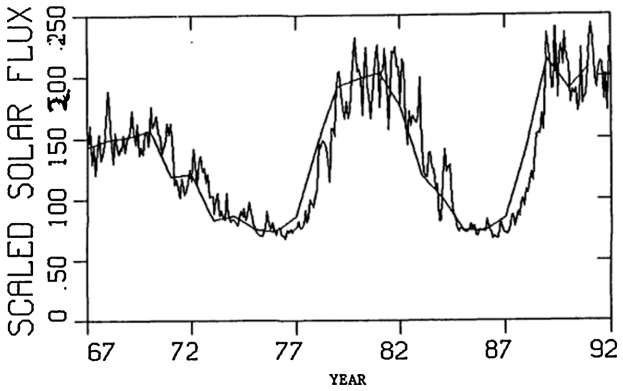

Figure 7. Monthly (overshoots and undershoots and annual (smooth) average values have been plotted.

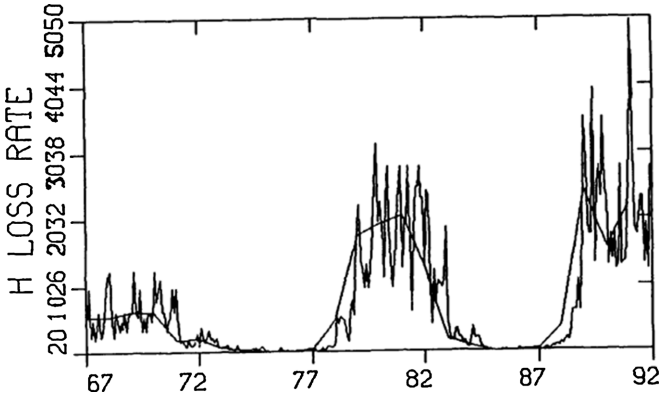

Figure 8. Monthly and annual average (smooth lines) values have been plotted.

[54]. More hydrogen escapes cause enhanced precipitation of low energy particles. Also, the depression of thermosphere toward the Earth may cause generation of more quasi-trapped particles in 1982. The average solar 10.7 cm radio flux during 1984-1986 was 80 and in 1982 was ~ 175 [53]. The exospheric temperature corresponding to these solar inputs was ~ 750˚ K in 1984-1986 and 1140˚ K in 1982 [55]. The Jeans hydrogen escape fluxes [54] corresponding to these temperatures were ~28 in 1984-1986 and ~750 in 1982. Since the majority of the observed particles are of the low energy region where charge exchange production predominates, it is likely that upward escaping gases enhanced the neutral generation, and consequently, increased the low altitude flux in 1982 or decreased the flux in 1984-1986.

5. Low- and Mid-latitude Data Processing and Analysis

5.1. Location of Peak Counting Rates in Latitude and χ Space

Figure 9(a) shows the distribution of the peak counting rates in latitude and χ, and Figure 9(b), that in B-L space for mid latitude protons only. The top plot helps to find the latitude ranges of locally mirroring protons in all the three zones. The maximum detection efficiency of the telescope for locally mirroring particles corresponding to $\chi = 90^{\circ}$ is shown in Figure 5(a) above.

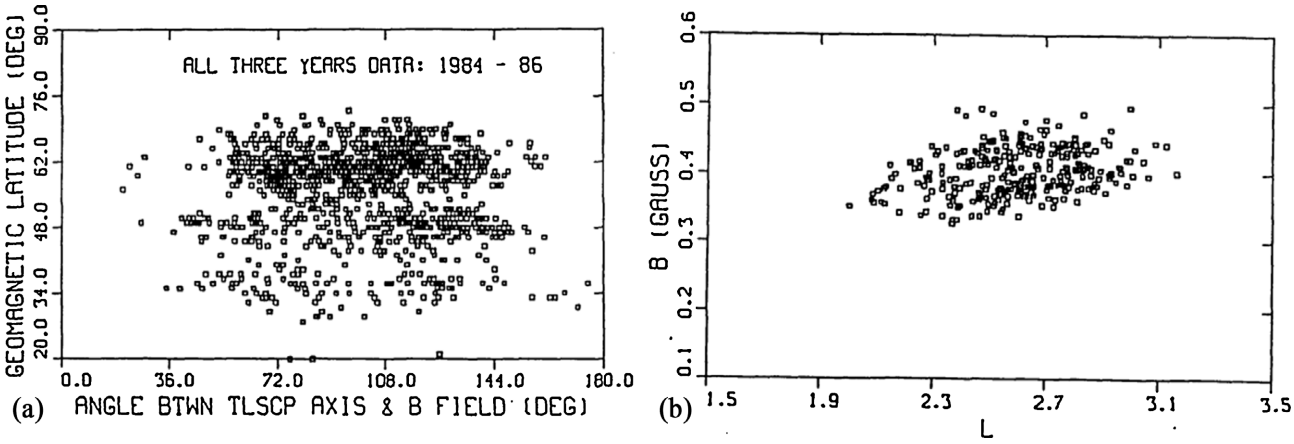

Figure 9. (a) The distribution of the peak counting rates in latitude and χ for the midlatitude protons; (b) The distribution of the peak counting rates in B-L space for the midlatitude protons.

5.2. Peak Counting Rates vs Telescope Inclination

Figure 10 shows such a plot for both protons and electrons in the mid-latitude zone. The plots show that the local mirroring particles outnumber particles of other pitch angles. The second peaks in the counting rates for $70^{\circ} < \chi < 80^{\circ}$ is thought to be due to the scattering by electromagnetic waves in the ionosphere. The response function depends on the telescope inclination with respect to the magnetic field, and so do the particle count rates.

5.3. *L*-Dependence

The *L*-range along the horizontal axis covers both the low-latitude and the mid-

latitude. It is found that the L-dependence is dominated by the telescope inclination, and so on the efficiency function, and the pitch angles of particles. This should be obvious because of the scattering effect by the telescope inclination electromagnetic waves generated in the ionosphere. Figures 11-15 show plots of the peak flux vs L. As said above, the dotted lines represents protons and the solid lines electrons. Figure 11(a) shows that for $85^\circ \le \chi \le 90^\circ$, in the low-latitude region, the electron peak lies in $2 \le L \le 2.2$, whereas the proton peak lies within 1.8 to 2.0. Further, in the mid-latitude region, proton peak lies within 2.2 and 2.4, and a second electron peak is not found before $L = 3$ - 3.2 which is thought to fall in the auroral region. It may be that some temporal effect has masked the electron peak in the mid-latitude region. Many such features are reflected in the plots through Figures 15(b).

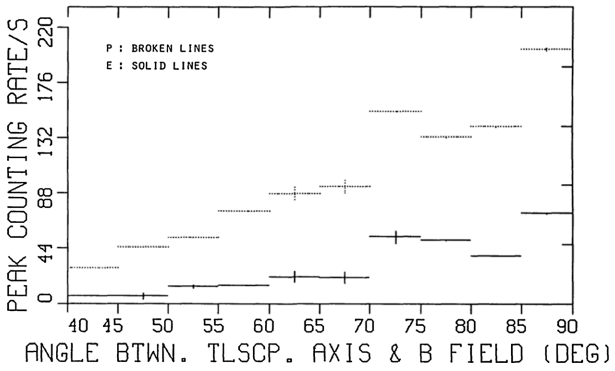

Figure 10. A plot for both protons and electrons in the mid-latitude zone.

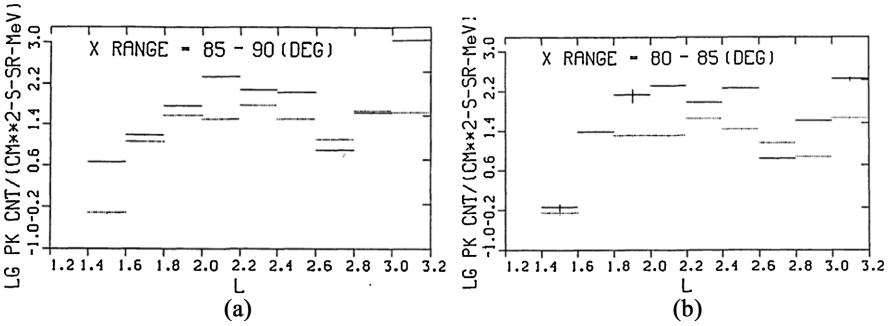

Figure 11. (a) Proton and electron fluxes vs L-values for χ range of 85˚ - 90˚; (b) Proton and electron fluxes vs L-values for χ range of 80˚ - 85˚.

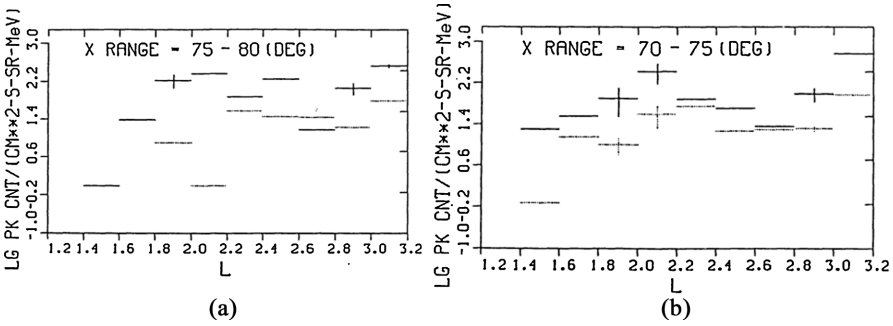

Figure 12. (a) Proton and electron fluxes vs L-values for χ range of 75˚ - 80˚; (b) Proton and electron fluxes vs L-values for χ range of 70˚ - 75˚.

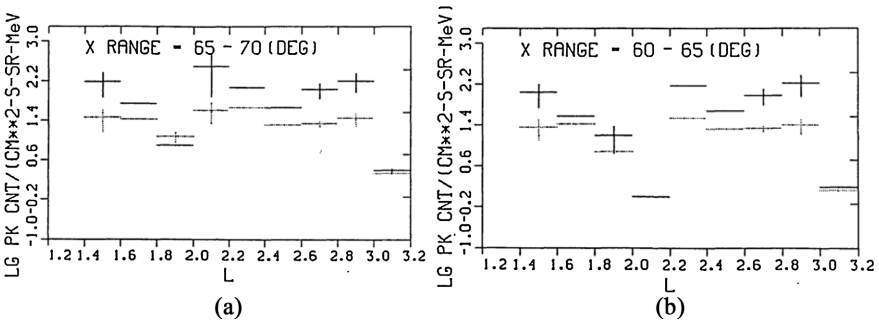

Figure 13. (a) Proton and electron fluxes vs L-values for χ range of 65˚ - 70˚; (b) Proton and electron fluxes vs L-values for χ range of 60˚ - 65˚.

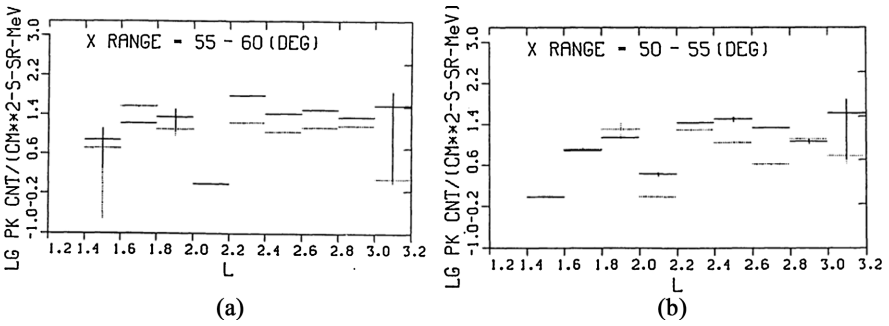

Figure 14. (a) Proton and electron fluxes vs L-values for χ range of 55˚ - 60˚; (b) Proton and electron fluxes vs L-values for χ range of 50˚ - 55˚.

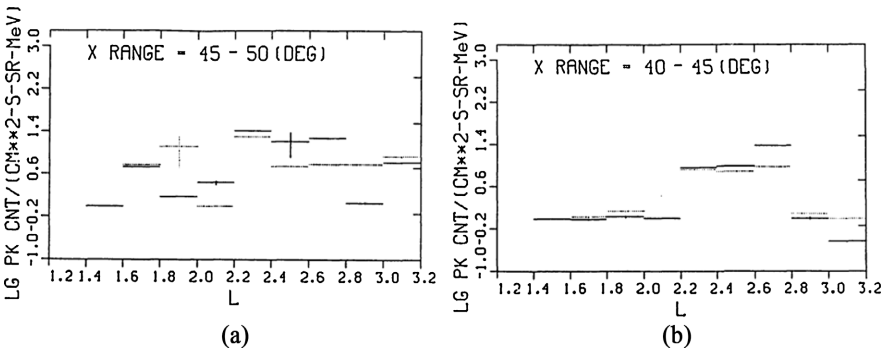

Figure 15. (a) Proton and electron fluxes vs L-values for χ range of 45˚ - 50˚; (b) Proton and electron fluxes vs L-values for χ range of 40˚ - 45˚.

5.4. Altitude Dependence

Figure 16(a) shows altitude dependence. There is a peak value within $650 \leq h \leq 700$ km. The bottom Figure 16(b) shows the plot of χ vs altitude. In this altitude range χ value is far away from χ corresponding to the maximum efficiency of the telescope. Any altitude covers the entire range of χ values in Figure 16(b). This feature needs to be investigated further.

5.5. Longitude Dependence

Figure 17(a) shows the longitude dependence. The drop in both electron and proton fluxes around 30˚ - 72˚ longitude bin is due to a few data points which is

evident from the bottom Figure 17(b). Within 140˚ - 360˚, longitude dependence is virtually absent. At any longitude all the χ-values are present.

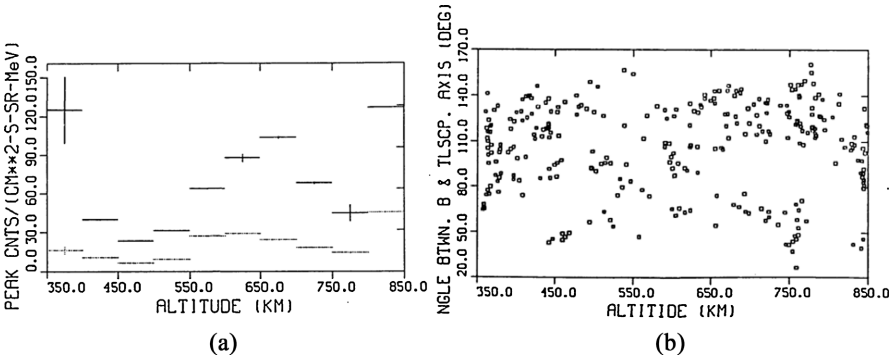

Figure 16. (a) Altitude dependence of proton and electron fluxes; (b) A plot of χ vs altitude.

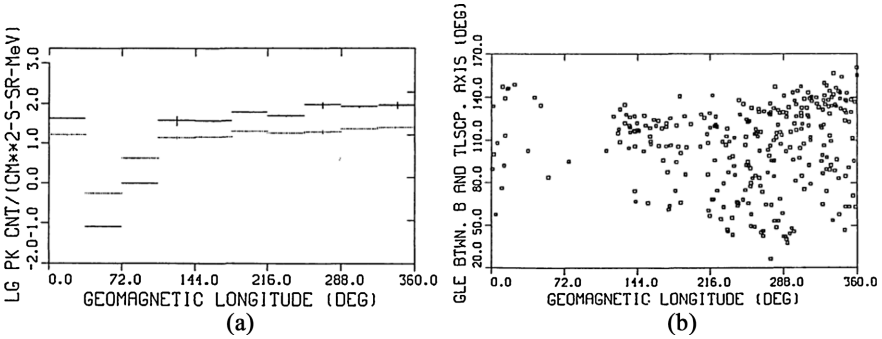

Figure 17. (a) Longitude dependence of flux; (b) Longitude dependence of flux

5.6. Temporal Features

An interesting effect is observed if we compare Figure 1(a) and Figure 1(b) with Figure 18(a) and Figure 18(b). The zeros along the horizontal line are to be ignored. The first set of figures shows the proton counting rates (broken line) are much lower than the electron counting rates (solid line). The second set of figures shows the opposite effect. Differences in longitudes cannot be a reason for the variation of counting rates. Either temporal or altitude variation or both factors may contribute to this effect.

5.7. Local Time Effect

Peak proton counting rates in the midlatitude region vs local time has been plotted in Figure 19(a), and the χ vs local time plotted in Figure 19(b). The reason for the low values of the peak counting rates in the local time range 10 - 14 hrs is due to the very high χ values (−1300 - 1600) and consequently very low instrumental efficiency during these hours (vide Figures 3(a)-(f)). It may be concluded that local time does not affect peak counting rates.

5.8. Energy Spectra

The differential energy spectra of both electrons (solid lines) and protons (dot-

ted lines) in the midlatitude region are shown in Figure 20 & Figure 21. These spectral shapes were common among previous observations which showed L dependent spectral shapes. Spectral shapes are also modulated by the minimum mirror altitude value of the particles. The spectral shapes may further be investigated for different L values and minimum mirror altitude ranges for further information.

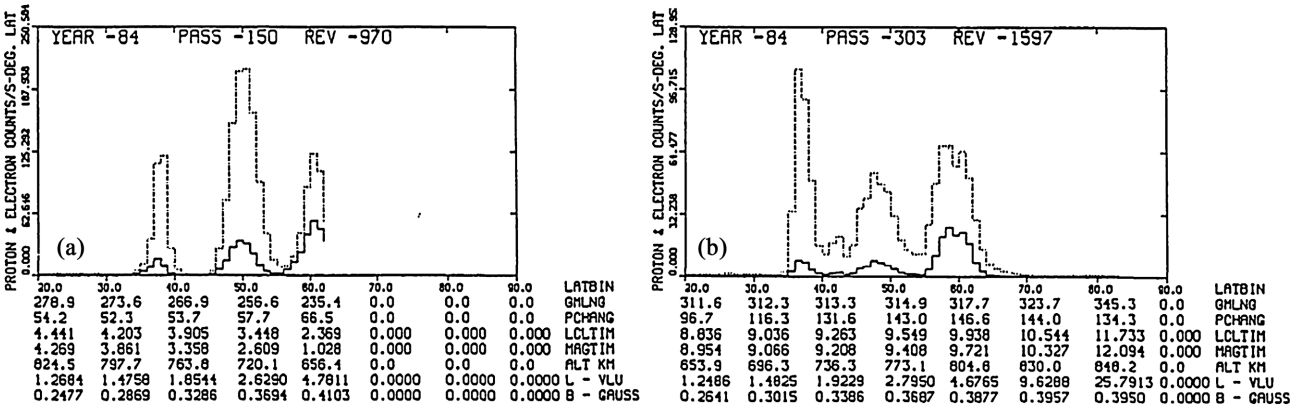

Figure 18. (a) Survey plot of electron and proton counting; (b) Survey plot of electron and proton counting.

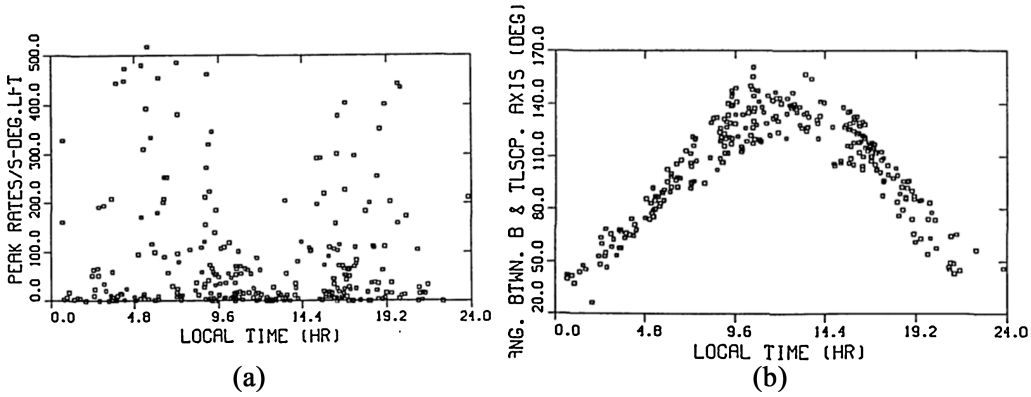

Figure 19. (a) Particle counting rates vs local time; (b) Plot of χ vs local time

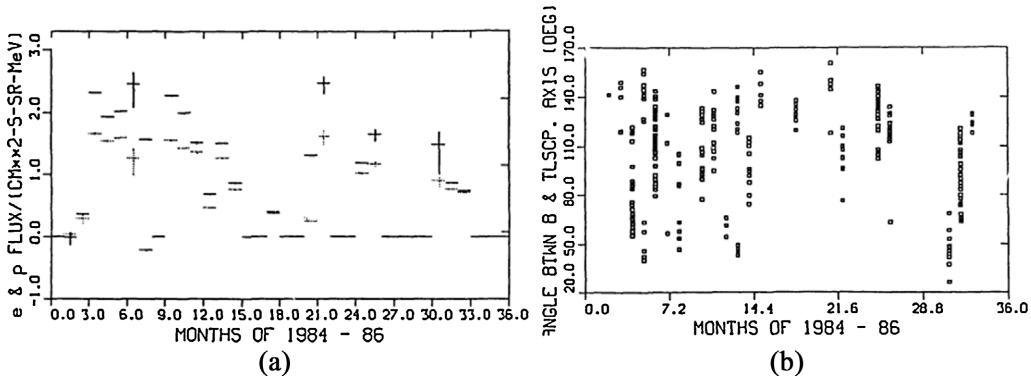

Figure 20. (a) Monthly variations of both protons (dotted lines) and electrons (solid lines) are plotted; (b) Illustrates that the repetitions of the relative variations of the maxima and minima of e and p fluxes are related to the χ angle or in other words to the instrumental efficiency.

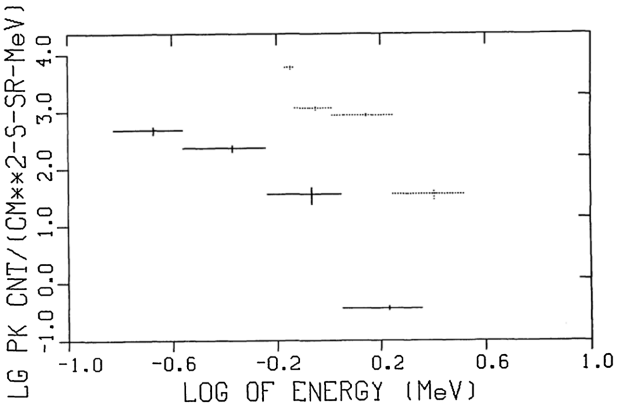

Figure 21. The differential energy spectra of both electrons (solid lines) and protons (dotted lines) in the midlatitude region are shown.

6. Conclusion

Particle precipitation over a period of about a decade has been described with increased features. The salient ones are that the global profiles of the peak counting rates in all the zones—the equatorial zone, the low-latitude zone, the mid-latitude, and the auroral zone—follow the minimum geomagnetic equator. At times the proton counting rates surpass the electron counting rates and at times the opposite happens. This article pertains to EXOS-C's LEO observations that use historical databases. The temporal variation of quasi-trapped proton population near the geomagnetic equator reveals that the peak value of the equatorially mirroring component may increase by a factor of 50 or more between a solar maximum and minimum conditions. Further, proton (0.64 - 32 MeV) and electron (0.19 - 3.2 MeV) populations in the said midlatitude zone show longitude and altitude dependencies. The locations of the peak profiles in all three zones in L-space depend upon the pitch angles of particles the distribution of which shows a second peak in addition to the one at 90˚ pitch angle. Particle flux does not depend on the local time. However, there is a great relative variation in e and p fluxes detected in the study of the seasonal variations, possibly due to the solar condition. Particle flux variations are indicative of the presence of scattering by electromagnetic waves generated in the ionosphere. Hopefully, the study falls in the NASA's encouragement for using historical databases from *in situ* spacecraft observations and/or extended low-Earth orbit (LEO) observations to build innovative data-based specification and prediction capabilities for the global magnetosphere through application of data assimilation tools and methods. Theoretical understanding of these observations is in progress with the work of data analysis of other parts of the global zones.

Statement

EXOS-C data was given to the author by Dr. Nagata in 1989-1990. Dr. Nagata's whereabouts were not found at the time of writing the article. Since full names of Dr. Nagata and his group members, were not available for mentioning in the pa-

per, their names were omitted.

Conflicts of Interest

The author declares no conflicts of interest.

References

[1] Zhang, J., Blanco-Cano, X., Nitta, N., Srivastava, N. and Mandrini, C.H. (2018) Editorial: Earth-Affecting Solar Transients. *Solar Physics*, **293**, Article No. 80. https://doi.org/10.1007/s11207-018-1302-9

[2] Gopalswamy, N. (2016) History and Development of Coronal Mass Ejections as a Key Player in Solar Terrestrial Relationship. *Geoscience Letters*, **3**, Article No. 8. https://doi.org/10.1186/s40562-016-0039-2

[3] Banu, S.A., Lugaz, N., Zhuang, B., Al-Haddad, N., Farrugia, C.J. and Galvin, A.B. (2025) Investigating Coronal Mass Ejections through Multispacecraft Measurements: STEREO-A and L1 in 2022-2023. *The Astrophysical Journal*, **982**, Article No. 47. https://doi.org/10.3847/1538-4357/adb60c

[4] Zhuang, B., Lugaz, N., Wood, B.E., Braga, C.R., Temmer, M., Gou, T., *et al.* (2025) Evolution of a Coronal Mass Ejection with an Eruptive Prominence from the Corona to Interplanetary Space. *The Astrophysical Journal*, **990**, Article No. 181. https://doi.org/10.3847/1538-4357/adf2a9

[5] Pal, S., Mac Cormack, C., Kilpua, E.K.J., Yogesh, Jian, L.K. and Nieves-Chinchilla, T. (2025) Magnetic Interaction Analysis of Multiple Interplanetary Coronal Mass Ejections That Led to a Historic Geomagnetic Storm in May 2024. *Astronomy & Astrophysics*, **702**, A150. https://doi.org/10.1051/0004-6361/202555908

[6] Mohil, M., Singh, S. and Jha, R. (2025) Hybrid LSTM-GRU Model for Predicting Solar Activity and Geomagnetic Indices. *Astrophysics and Space Science*, **370**, Article No. 118. https://doi.org/10.1007/s10509-025-04510-y

[7] Möstl, C., Davies, E.E., Weiler, E., Rüdisser, H.T., Amerstorfer, U.V., Weiss, A.J., *et al.* (2026) On the Magnetic Field Evolution of Interplanetary Coronal Mass Ejections from 0.07 to 5.4 Au. *The Astrophysical Journal*, **1001**, Article No. 70. https://doi.org/10.3847/1538-4357/ae50fe

[8] Lamy, P., Boursier, Y. Loirat, J. and Zhukov, A. (2025) Three-Dimensional Reconstruction and Propagation of an Asymmetric Flux-Rope Coronal Mass Ejection.

[9] Rüdisser, H.T., Nguyen, G., Le Louëdec, J., Davies, E.E. and Möstl, C. (2026) ARCANE-Early Detection of Interplanetary Coronal Mass Ejections. *Space Weather*, **24**, e2025SW004537. https://doi.org/10.1029/2025sw004537

[10] Rüdisser, H.T., Davies, E.E., Amerstorfer, U.V., *et al.* (2026) Towards a Fully Automated Pipeline for Short-Term Forecasting of *in Situ* Coronal Mass Ejection Magnetic Field Structure.

[11] Mannucci, A.J., Tsurutani, B.T., Iijima, B.A., Komjathy, A., Saito, A., Gonzalez, W.D., *et al.* (2005) Dayside Global Ionospheric Response to the Major Interplanetary Events of October 29-30, 2003 "Halloween Storms". *Geophysical Research Letters*, **32**, L12S02. https://doi.org/10.1029/2004gl021467

[12] Tsurutani, B.T. and Lakhina, G.S. (2014) An Extreme Coronal Mass Ejection and Consequences for the Magnetosphere and Earth. *Geophysical Research Letters*, **41**, 287-292. https://doi.org/10.1002/2013gl058825

[13] Hayakawa, H., Ebihara, Y., Mishev, A., Koldobskiy, S., Kusano, K., Bechet, S., *et al.* (2025) The Solar and Geomagnetic Storms in 2024 May: A Flash Data Report. *The*

Astrophysical Journal, **979**, Article No. 49.
https://doi.org/10.3847/1538-4357/ad9335

[14] Li, G., Zank, G.P. and Rice, W.K.M. (2003) Energetic Particle Acceleration and Transport at Coronal Mass Ejection-Driven Shocks. *Journal of Geophysical Research*: *Space Physics*, **108**, Article No. 1082. https://doi.org/10.1029/2002ja009666

[15] Tsurutani, B., Mannucci, A., Iijima, B., Abdu, M.A., Sobral, J.H.A., Gonzalez, W., *et al*. (2004) Global Dayside Ionospheric Uplift and Enhancement Associated with Interplanetary Electric Fields. *Journal of Geophysical Research*: *Space Physics*, **109**, A08302. https://doi.org/10.1029/2003ja010342

[16] Tsurutani, B.T., Verkhoglyadova, O.P., Mannucci, A.J., Saito, A., Araki, T., Yumoto, K., *et al*. (2008) Prompt Penetration Electric Fields (PPEFs) and Their Ionospheric Effects during the Great Magnetic Storm of 30-31 October 2003. *Journal of Geophysical Research*: *Space Physics*, **113**, A05311. https://doi.org/10.1029/2007ja012879

[17] Zong, Q., Reinisch, B.W., Song, P., Wei, Y. and Galkin, I.A. (2010) Dayside Ionospheric Response to the Intense Interplanetary Shocks-solar Wind Discontinuities: Observations from the Digisonde Global Ionospheric Radio Observatory. *Journal of Geophysical Research*: *Space Physics*, **115**, A06304.
https://doi.org/10.1029/2009ja014796

[18] Liu, Y.D., Hu, H., Wang, R., Yang, Z., Zhu, B., Liu, Y.A., *et al*. (2015) Plasma and Magnetic Field Characteristics of Solar Coronal Mass Ejections in Relation to Geomagnetic Storm Intensity and Variability. *The Astrophysical Journal*, **809**, L34.
https://doi.org/10.1088/2041-8205/809/2/l34

[19] Baker, D.N., Jaynes, A.N., Kanekal, S.G., Foster, J.C., Erickson, P.J., Fennell, J.F., *et al*. (2016) Highly Relativistic Radiation Belt Electron Acceleration, Transport, and Loss: Large Solar Storm Events of March and June 2015. *Journal of Geophysical Research*: *Space Physics*, **121**, 6647-6660. https://doi.org/10.1002/2016ja022502

[20] Baker, D.N., Jaynes, A.N., Turner, D.L., Nakamura, R., Schmid, D., Mauk, B.H., *et al*. (2016) A Telescopic and Microscopic Examination of Acceleration in the June 2015 Geomagnetic Storm: Magnetospheric Multiscale and Van Allen Probes Study of Substorm Particle Injection. *Geophysical Research Letters*, **43**, 6051-6059.
https://doi.org/10.1002/2016gl069643

[21] Reiff, P.H., Daou, A.G., Sazykin, S.Y., Nakamura, R., Hairston, M.R., Coffey, V., *et al*. (2016) Multispacecraft Observations and Modeling of the 22/23 June 2015 Geomagnetic Storm. *Geophysical Research Letters*, **43**, 7311-7318.
https://doi.org/10.1002/2016gl069154

[22] Liu, Y., Fu, L., Wang, J. and Zhang, C. (2018) Studying Ionosphere Responses to a Geomagnetic Storm in June 2015 with Multi-Constellation Observations. *Remote Sensing*, **10**, Article No. 666. https://doi.org/10.3390/rs10050666

[23] Liu, G., Huang, W., Shen, H., Aa, E., Li, M., Liu, S., *et al*. (2019) Ionospheric Response to the 2018 Sudden Stratospheric Warming Event at Middle- and Low-Latitude Stations over China Sector. *Space Weather*, **17**, 1230-1240.
https://doi.org/10.1029/2019sw002160

[24] Venkatesh, K., Tulasi Ram, S., Fagundes, P.R., Seemala, G.K. and Batista, I.S. (2017) Electrodynamic Disturbances in the Brazilian Equatorial and Low-Latitude Ionosphere on St. Patrick's Day Storm of 17 March 2015. *Journal of Geophysical Research*: *Space Physics*, **122**, 4553-4570. https://doi.org/10.1002/2017ja024009

[25] Astafyeva, E., Zakharenkova, I. and Alken, P. (2016) Prompt Penetration Electric Fields and the Extreme Topside Ionospheric Response to the June 22-23, 2015 Geomagnetic Storm as Seen by the Swarm Constellation. *Earth, Planets and Space*, **68**,

Article No. 152. https://doi.org/10.1186/s40623-016-0526-x

[26] Anastasiadis, A., Papaioannou, A., Sandberg, I., Georgoulis, M., Tziotziou, K., Kouloumvakos, A., *et al.* (2017) Predicting Flares and Solar Energetic Particle Events: The FORSPEF Tool. *Solar Physics*, **292**, Article No. 134. https://doi.org/10.1007/s11207-017-1163-7

[27] Belakhovsky, V.B., Pilipenko, V.A., Antonova, E.E., Miyoshi, Y., Kasahara, Y., Kasahara, S., *et al.* (2023) Relativistic Electron Flux Growth during Storm and Non-Storm Periods as Observed by ARASE and GOES Satellites. *Earth, Planets and Space*, **75**, Article No. 189. https://doi.org/10.1186/s40623-023-01925-1

[28] Kalegaev, V.V., Ivanova, A.R., Gruzdov, D.S., Vlasova, N.A., Bazilevskaya, G.A. and Makhmutov, V.S. (2023) Energetic Electrons Precipitation into the Earth's Atmosphere during Magnetic Storm on 1-5 February 2015. In: Kosterov, A., *et al.*, Eds., *Springer Proceedings in Earth and Environmental Sciences*, Springer International Publishing, 301-312. https://doi.org/10.1007/978-3-031-40728-4_22

[29] Gao, L., Shen, C., Zhou, Y., Ji, Y., Pu, Z., Parks, G., *et al.* (2024) Observational Features of Charge Distribution in Earth's Inner Magnetosphere. *Communications Physics*, **7**, Article No. 63. https://doi.org/10.1038/s42005-024-01553-5

[30] Papaioannou, A., Sandberg, I., Anastasiadis, A., Kouloumvakos, A., Georgoulis, M.K., Tziotziou, K., *et al.* (2016) Solar Flares, Coronal Mass Ejections and Solar Energetic Particle Event Characteristics. *Journal of Space Weather and Space Climate*, **6**, A42. https://doi.org/10.1051/swsc/2016035

[31] Laurenza, M., Cliver, E.W., Hewitt, J., Storini, M., Ling, A.G., Balch, C.C., *et al.* (2009) A Technique for Short-Term Warning of Solar Energetic Particle Events Based on Flare Location, Flare Size, and Evidence of Particle Escape. *Space Weather*, **7**, S04008. https://doi.org/10.1029/2007sw000379

[32] Tsyganenko, N.A. and Sitnov, M.I. (2005) Modeling the Dynamics of the Inner Magnetosphere during Strong Geomagnetic Storms. *Journal of Geophysical Research: Space Physics*, **110**, A03208. https://doi.org/10.1029/2004ja010798

[33] Sun, X., Zhima, Z., Duan, S., Hu, Y., Lu, C. and Ran, Z. (2024) Statistical Analysis of the Correlation between Geomagnetic Storm Intensity and Solar Wind Parameters from 1996 to 2023. *Remote Sensing*, **16**, Article No. 2952. https://doi.org/10.3390/rs16162952

[34] Biswas, S., Bhaskar, A., Abitha, S.G., *et al.* (2026) Unprecedented Multipoint Observation of Spatially Varying ICME Turbulence of Different Ages during October 2024 Extreme Solar Storm at 1 AU.

[35] Davies, E.E., Weiler, E., Möstl, C., *et al.* (2025) Real-Time Prediction of Geomagnetic Storms Using Solar Orbiter as a Far Upstream Solar Wind Monitor. *ESS Open Archive*. https://doi.org/10.22541/essoar.175580321.18096327/v1

[36] European Space Agency (ESA) (2021) ACE (Advanced Composition Explorer)—Mission Status. ESA eoPortal Directory. https://directory.eoportal.org/web/eoportal/satellite-missions/a/ace

[37] Strickland, A. (2025) Voyager 1 Will Reach One Light-Day from Earth in 2026. Here's What That Means. https://www.cnn.com/2025/12/09/science/voyager-1-light-day-earth#:~:text=By-Ashley%20Strickland,-DEC%209%2C%202025

[38] Smith, P.H. and Bewtra, N.K. (1976) Dependence of the Charge Exchange Lifetimes on Mirror Latitude. *Geophysical Research Letters*, **3**, 689-692. https://doi.org/10.1029/gl003i011p00689

[39] Cornwall, J.M., Coroniti, F.V. and Thorne, R.M. (1970) Turbulent Loss of Ring Current Protons. *Journal of Geophysical Research*, **75**, 4699-4709. https://doi.org/10.1029/ja075i025p04699

[40] Williams, D.J., Hernandez, G. and Lyons, L.R. (1976) Simultaneous Observations of the Proton Ring Current and Stable Auroral Red Arcs. *Journal of Geophysical Research*, **81**, 608-616. https://doi.org/10.1029/ja081i004p00608

[41] Mizera, P.F. and Blake, J.B. (1973) Observations of Ring Current Protons at Low Altitudes. *Journal of Geophysical Research*, **78**, 1058-1062. https://doi.org/10.1029/ja078i007p01058

[42] Hovestadt, D., Häusler, B. and Scholer, M. (1972) Observation of Energetic Particles at Very Low Altitudes near the Geomagnetic Equator. *Physical Review Letters*, **28**, 1340-1344. https://doi.org/10.1103/physrevlett.28.1340

[43] Moritz, J. (1972) Energetic Protons at Low Equatorial Altitudes: A Newly Discovered Radiation Belt Phenomenon and Its Explanation. *Zeitschrift für Geophysik*, **38**, 701-717.

[44] Scholer, M., Hovestadt, D. and Morfill, G. (1975) Energetic He^+ Ions from the Radiation Belt at Low Altitudes near the Geomagnetic Equator. *Journal of Geophysical Research*, **80**, 80-85. https://doi.org/10.1029/ja080i001p00080

[45] Fischer, H.M., Auschrat, V.W. and Wibberenz, G. (1977) Angular Distribution and Energy Spectra of Protons of Energy $5 \leq e \leq 50$ Mev at the Lower Edge of the Radiation Belt in Equatorial Latitudes. *Journal of Geophysical Research*, **82**, 537-547. https://doi.org/10.1029/ja082i004p00537

[46] Claflin, E.S. and White, R.S. (1974) A Study of Equatorial Inner Belt Protons from 2 to 200 Mev. *Journal of Geophysical Research*, **79**, 959-965. https://doi.org/10.1029/ja079i007p00959

[47] Parsignault, D.R., Holeman, E. and Filz, R.C. (1981) Long-Term Intensity Decrease in the 8- to 25-MeV Proton Fluxes at Low *L* Values. *Journal of Geophysical Research: Space Physics*, **86**, 11447-11450. https://doi.org/10.1029/ja086ia13p11447

[48] Miah, M.A. (1989) Observation of Low Energy Particle Precipitation at Low Altitude in the Equatorial Zone. *Journal of Atmospheric and Terrestrial Physics*, **51**, 541-549. https://doi.org/10.1016/0021-9169(89)90094-9

[49] Miah, M.A. (1991) Global Proton Peak Flux Profile in the Equatorial Zone. *Indian Journal of Radio and Space Science*, **20**, 12-24.

[50] Miah, M.A. (1991) The ONR-602 Experiment and Investigation of Particle Precipitation near the Equator. *Journal of Geomagnetism and Geoelectricity*, **43**, 445-460. https://doi.org/10.5636/jgg.43.445

[51] Miah, M.A., Nagata, K., Kohno, T., Murakami, H., Nakamoto, A., Hasebe, N., *et al.* (1992) Spatial and Temporal Features of 0.64-35 MeV Protons in the Space Station Environment: EXOS-C Observations. *Journal of Geomagnetism and Geoelectricity*, **44**, 591-610. https://doi.org/10.5636/jgg.44.591

[52] Miah, M.A. (1991) Observation of $Z \geq 1$ Particles Below 300 km near the Geomagnetic Equator. *Journal of Geomagnetism and Geoelectricity*, **43**, 461-475. https://doi.org/10.5636/jgg.43.461

[53] Coffey, H. (1992) NOAA, Boulder, Colorado, Private Communication.

[54] Fahr, H.J. and Shizgal, B. (1983) Modern Exospheric Theories and Their Observational Relevance. *Reviews of Geophysics*, **21**, 75-124. https://doi.org/10.1029/rg021i001p00075

[55] Jacchia, L.G. (1977) Thermospheric Temperature, Density, and Composition: New Models. Smithsonian Astrophysical Observatory, Special Report No. 375.